Nonlinear Processes in Geophysics (1995) 2: 158 - 177

Nonlinear Processes in Geophysics

Organisation of joints and faults from 1-cm to 100-km scales revealed by optimized anisotropic wavelet coefficient method and multifractal analysis

G. Ouillon[1,2,3], D. Sornette[3] and C. Castaing[2]

[1] Institut de Géodynamique, CNRS URA 1279, Rue A. Einstein, Sophia Antipolis, 06560 Vabonne, France
[2] BRGM, Avenue de Concyr, Orléans-La Source (Loiret), B.P. 6009, 45060 Orléans Cedex 2, France
[3] Laboratoire de Physique de la Matière Condensée, CNRS URA 190, Université de Nice-Sophia Antipolis, B.P. 70, Parc Valrose, 06108 Nice Cedex 2, France

Received 27 September 1994 - Accepted 16 December 1994 - Communicated by A. Provenzale

Abstract. The classical method of statistical physics deduces the macroscopic behaviour of a system from the organization and interactions of its microscopical constituants. This kind of problem can often be solved using procedures deduced from the Renormalization Group Theory, but in some cases, the basic microscopic rules are unknown and one has to deal only with the intrinsic geometry. The wavelet analysis concept appears to be particularly adapted to this kind of situation, as it highlights details of a set at a given analyzing scale. As fractures and faults generally define highly anisotropic fields, we defined a new renormalization procedure based on the use of anisotropic wavelets. This approach consists of finding an optimum filter which maximizes wavelet coefficients at each point of the field. Its intrinsic definition allows us to compute a rose diagram of the main structural directions present in the field at every scale. Scaling properties are determined using a multifractal box-counting analysis improved to take account of samples with irregular geometry and finite size. In addition, we present histograms of fault length distribution. Our main observation is that different geometries and scaling laws hold for different ranges of scales, separated by boundaries that correlate well with thicknesses of lithological units that constitute the continental crust. At scales involving the deformation of the crystalline crust, we find that faulting displays some singularities similar to those commonly observed in Diffusion-Limited Aggregation processes.

1 Introduction

Since the development of modern physics of many-body systems, a lot of work has been done to estimate the macroscopic behaviour of a system from the knowledge of its microscopic properties and elementary interactions. The main question is to determine how much of the microscopic details survive and control the macroscopic behaviour. In most cases, a 'renormalization' occurs such that only broad global properties control the large scale properties and most of the microscopical details are 'washed out'. There are basically two well-known classes of such renormalization. Here we want to introduce a third one. The champion of the first class is the ideal gas: assuming a Boltzmann distribution of the molecules velocities depending on the temperature, one can derive the well-known equilibrium equation relating pressure P, temperature T and volume V of a gas mole: $PV = RT$, where R is the Joule constant (Diu et al, 1989). A more subtle renormalization occurs (the second class) when simple averaging or mean-field renormalization procedures breaks down. The typical example is provided by critical phenomena, which exhibit long-range correlations (Yeomans, 1992; Chandler, 1987), and can be described by fractal and multifractal measures. Macroscopic behaviour can then be deduced using methods belonging to the Renormalization Group (Wilson, 1983; Yeomans, 1992). The success of the Renormalization Group is based on *a priori* knowledge of the interactions between elementary objects constituting the global system. If those microscopical rules were not available, one needs to assume them. The aim of this paper is to present a third class of renormalization procedure, purely founded on geometrical analysis which is ideally suited to problems in which the basic interaction rules are unknown. We shall concentrate on a two-dimensional spatial problem (*i.e.* fracturing), but our approach can be extended to other more general cases. Our new method is based on passband filtering, using a family of filters called *wavelets*. We will first present and use isotropic filters (like many other workers in pattern recognition and image processing). Simple arguments will then show that the use of anisotropic wavelets is unavoidable, in spite of the larger quantity of information to be dealt with. This leads us to the definition of a new algorithm which gives us a series of objective representations of a microscopically

Correspondence to: G. Ouillon

known field at increasing scales. Applied to fault maps, we are able to define renormalized rupture lines, representing the fracture field at larger and larger scales. This method also allows us to compute renormalized rose diagrams of the orientations of the main field features, at all observation scales. A simple application is first carried on a synthetic model of *en échelon* faults to demonstrate the relevance of our analysis. As this method, that we call *Optimum Anisotropic Wavelet Coefficient Method* (OAWCM), is purely geometrical, we will complement our analysis with a study of the scaling properties of fault networks, using multifractal box-counting. This approach is inspired by the fact that self-similar properties of faulting have often been reported in the litterature (Mandelbrot et al, 1984; Scholz and Aviles, 1986; Herrmann and Roux, 1990; Sornette et al, 1990; Sornette, 1991; Kagan, 1991), suggesting that a single physical mechanism holds at every scale. This assumption, if true, would justify the use of some fault properties over a wide range of scales, thus allowing for instance the computation of strain and energy of the fault populations by extrapolation to unobservable-size domains (Scholz and Cowie, 1990). The method we use was conceived to correct measurements from irregular border sampling or finite size effects. This leads us to obtain more precise critical exponents of the two-dimensional organization of fault networks. In particular, we show that some fractal dimensions may be artefacts resulting solely from irregular sampling and finite size effects. Finally, frequency-length histogram estimations for faults provide insight into the growth process of a fault in a continental plate.

The area chosen for data collection was the sedimentary cover of the western Arabian plate (Fig. 1), due to the good exposure of joints and faults and the fairly well-defined tectonic boundary conditions. The plate consists of a Proterozoic basement deformed during the Pan-African orogeny over which lie Phanerozoic sediments as well as volcanic rocks.

The Pan-African orogeny was marked during its closing stages by the development of a broad zone of strike-slip faults, the Najd Fault System (Husseini, 1989). These faults strongly influenced the fracture pattern affecting the sedimentary cover. The WNW-ESE faults in Fig. 2 are due to this influence. The plate is surrounded by varied tectonic conditions: collision to the N-NE (Taurus-Zagros area), spreading centers of Gulf of Aden and Red Sea to the S-SE, and Dead Sea transform to the W. Displacement of the plate along the sinistral Dead Sea transform was estimated to be 105 km since the Miocene (Freund et al, 1970). During the Quaternary, the plate was submitted to an approximately NS compressive principal stress (Giannérini et al, 1988). The focus of our study is located in the thick Paleozoic platform, where accurate field mapping was carried out in the Tayma area. This area is characterized

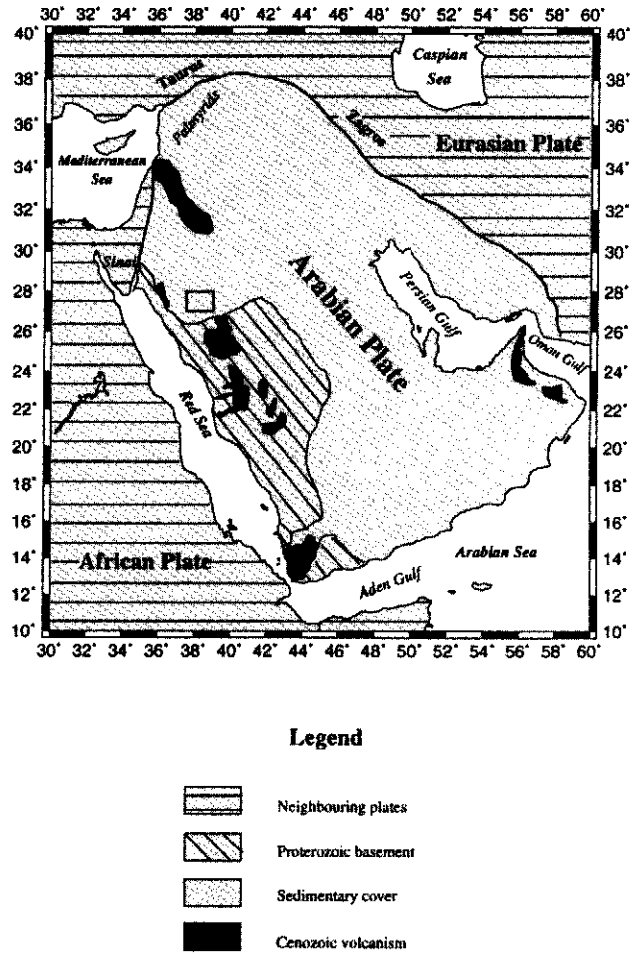

Fig. 1: Geological setting of the area under study. The Tayma area is located within the frame north of the outcroping proterozoic basement. It coincides with the dashed frame on Map VI (see Fig. 2).

by the outcropping Cambrian-Ordovician Saq sandstone formation. Moreover, interpretation and digitization of photographs taken from helicopter, classical aerial photographs as well as satellite images allow us to create a series of fracture network maps spanning a wide range of scales (from 1:1 to 1:1,000,000). Fig. 2 presents our dataset (each map being reduced after digitization to allow publication on a single page). Note that data were acquired following a zoom strategy. Space filling and anisotropy properties of each network were then studied with different methods, to define structural features that control fault network growth in a continental plate.

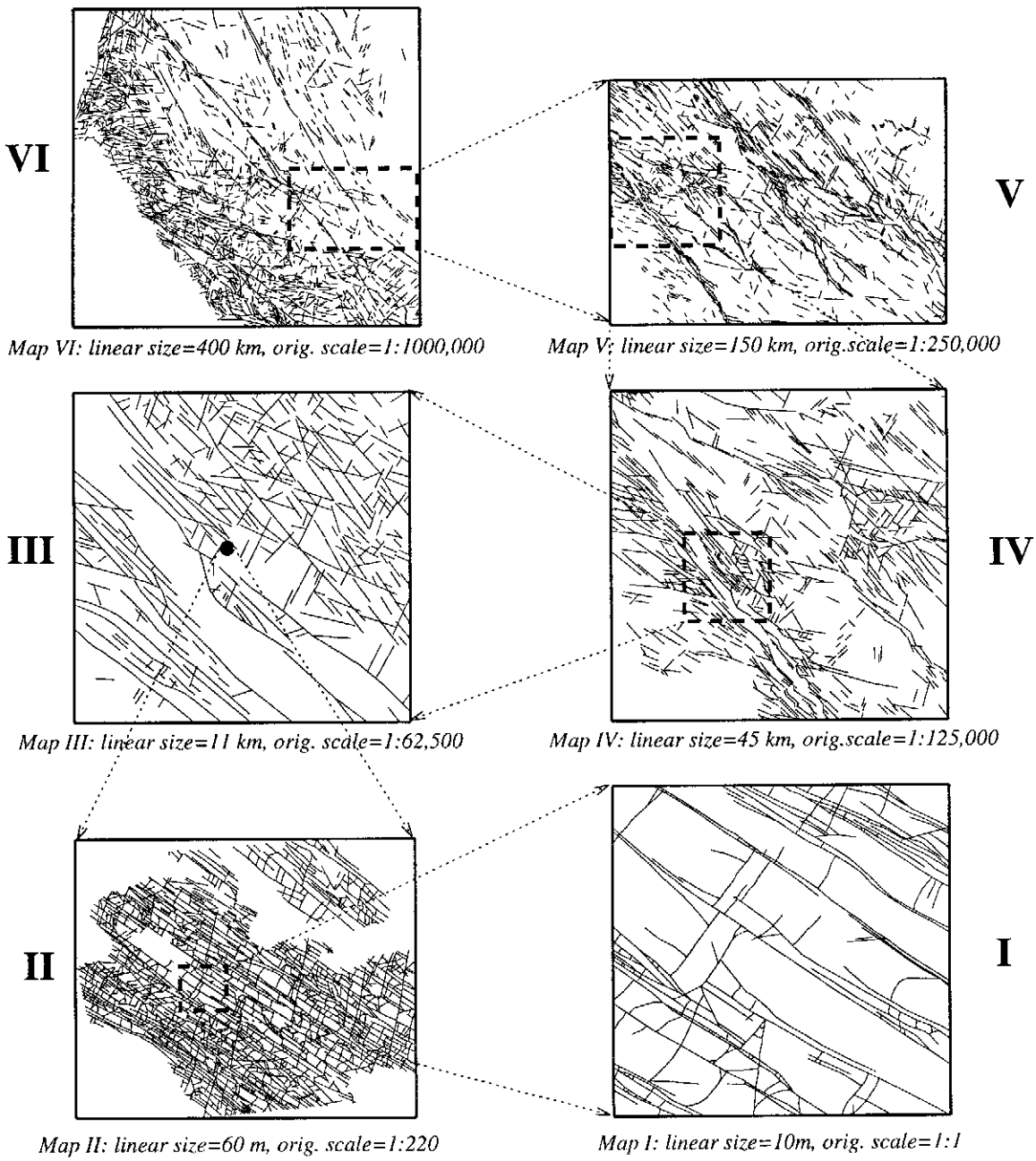

Fig. 2: Fracture networks used for this study. Dashed frames and arrows show the zoom process used during data acquisition. For instance, Map V is a zoom of the area within the dashed frame in Map VI. Similarly, Map II is a zoom of Map III at the location of the full circle. Legend under figures indicates the largest size of the image and the original scale at which fracture patterns were mapped.

2 The two-dimensional wavelet analysis

The wavelet transform was introduced in its present formalism for the first time in the middle of the eighties (Grossmann and Morlet, 1984). Large sections about the potential applications of this method can be found in the book of Meyer (1992). Most of the theoretical developments we shall present can be found there. Briefly, the aim of the wavelet transform is to decompose a signal into details of various scales, using a battery of filters called *wavelets*, derived from a single *mother function* Ψ. This mother wavelet must always be chosen so as to be well localized both in space and frequency. A *wavelet coefficient* is then defined at each point $\vec{b}$ of the signal I under study:

$$C_I(\vec{b}, a, \theta) = \frac{1}{K_\Psi} a^{-1} \int \Psi(R_\theta^{-1}(\frac{\vec{x} - \vec{b}}{a}))I(\vec{x})d\vec{x} \quad (1)$$

where R_θ is the counterclockwise rotation operator of angle θ with respect to the Ox axis, which allows to rotate the analyzing wavelet. The positive real parameter a is the central parameter. It allows us to dilate (high a) or to contract (low a) the wavelet, to analyze the signal with either a fine or a coarse resolution. The K_Ψ factor is defined as follows (*admissibility condition*):

$$K_\Psi = \int |\Psi^*(\vec{k})|^2 |\vec{k}|^{-2} d^2\vec{k} \quad (2)$$

where Ψ^* is the Fourier transform of Ψ. K_Ψ must remain finite, which implies that the wavelet has a zero-mean. So, it has the property of deleting constant level portions of the analyzed signal. A frequently used wavelet is the so-called *Mexican Hat*, which is the second derivative of the Gaussian function. Its analytical expression is (see also Fig. 3a):

$$\Psi(x, y) = (2 - (x^2 + y^2))e^{-\frac{1}{2}(x^2+y^2)} \quad (3)$$

This wavelet is of course isotropic.

Anisotropy can be introduced through the aspect ratio σ of the wavelet. We can then define the following mother filter (see Fig. 3b):

$$\Psi(x, y) = (2 - (\frac{x^2}{\sigma^2} + y^2))e^{-\frac{1}{2}(\frac{x^2}{\sigma^2}+y^2)} \quad (4)$$

By setting σ to unity, we recover the Mexican Hat filter.

Using equations (2) and (4), it can be shown (Ouillon, 1995) that the associated normalizing factor K_Ψ depends linearly on σ. For a given resolution a, a simple frequency analysis reveals that the anisotropic Mexican Hat gives the strongest contrast to structures of width $2.2a$ and of length $2.2\sigma a$ (Ouillon, 1995).

The numerical implementation of the wavelet transform is simple. Once the analyzing wavelet has been chosen, we choose the scale a of analysis and compute

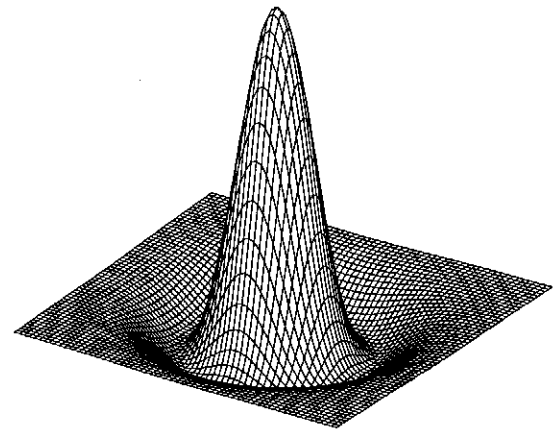

Fig. 3a: Isotropic Mexican hat wavelet discretized in a 64 by 64 mesh world.

the Fast Fourier Transform (FFT) of the wavelet and of the signal. The product of both spectra is computed, and the inverse FFT gives us the desired convolution map. Of course, edge effects do occur. The main one is due to the periodic nature of both the signal and the wavelet, implied by the Fourier transform method. To avoid it, we pre-process the original image as follows (Arnéodo, personal communication): first, it is sampled in a 256 by 256 matrix form. Then, this matrix is placed at the center of an empty 512 by 512 matrix. The filter is sampled in a 512 by 512 matrix form. The procedure starts with these two inputs. Edge effects are not completely eliminated, because the spatial domain of the wavelet does not always fit with the signal's domain. In practice, edge effects could be controlled with the use of compact wavelets, but those filters suffer from poor localization in the wavevector space. On the other hand, the use of wavelets highly localized in frequency implies that the wavelets are of infinite extent (this is the case for the Mexican Hat filter, for instance). No systematic rules exist, it and the user must judge when results are spurious.

3 Isotropic wavelet analysis of synthetic *en échelons* fractures

We shall first concentrate on the use of isotropic wavelets. Since much work and many examples can be found in the literature, we shall focus here on a simple case which consists of a synthetic well-known geological situation: *en échelons* fractures (see Fig. 4). This example is characterized by a scale dependent geometrical behaviour. At the 'microscopic' scale, we can detect small segments striking North/South, their centers being aligned in the N45E azimuth. At the 'macroscopic' scale, the only feature we perceive is a simple line, striking N45E. We presently show how to deduce this macroscopic behaviour from the known microscopic

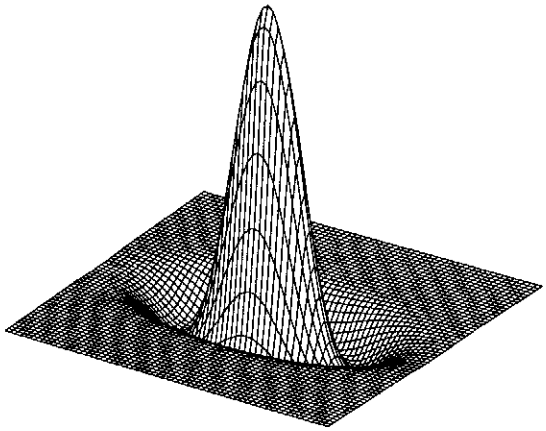

Fig 3b.: Anisotropic Mexican hat wavelet discretized in a 64 by 64 mesh world. The long to small axis ratio is 4.

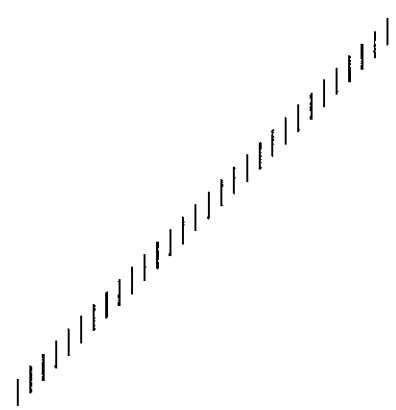

Fig. 4: Synthetic *en échelon* fractures.

geometry and see that the wavelet transform is a natural tool to process such a transformation. Fig. 5 presents the wavelet analysis of Fig. 4 at different resolutions: 2, 4, 8, 16 and 32 pixels. The wavelet we used is the isotropic Mexican Hat (equation (3)). Each segment is 16 pixels long. The spacing between segments is 8 pixels. At high resolutions (2 and 4 pixels), we still detect the microscopic constitution. The 8 pixels analysis lies at the transition to the macroscopic behaviour, where the large scale structure becomes apparent. This result is satisfactory, but it seems more natural that an anisotropic object has to be filtered with an anisotropic filter. The next part of this paper will discuss this idea.

4 The anisotropic wavelet analysis

We now show the influence of the azimut (θ angle) in an anisotropic analysis. Consider Fig. 6, with 2 segments of equal length, striking in directions defining a right angle. Each segment is 32 pixels long. The analyzing wavelet is now the anisotropic Mexican Hat (equation (4)), with $a = 4$ and $\sigma = 2$. Fig. 7a and 7b show the results of two different analyses: one with $\theta = 0$ (the long axis of the wavelet horizontal), the other with $\theta = \pi/2$ (the long axis vertical). An inspection of the result leads us to the conclusion that in each case the segment corresponding to the wavelet azimut is highlighted, relative to the other. For a similar analysis, see also the work of Antoine (1992). We have also checked the behaviour of the wavelet coefficient at the center of a segment as a function of σ (the azimut of the wavelet is kept equal to that of the segment). The wavelet coefficient reaches its maximum when wavelet's size corresponds to the length of the segment (see also Section 2). This encourages us to think that, in a nonstationary signal, each point must be associated with a specific filter that gives an optimal response. In our problem, this filter has size and orientation specifications that can vary from point to point. These specifications correspond in fact to the size and orientation of the structures surrounding each point of the signal. Moreover, simple arithmetics lead us to a dramatic material situation: imagine we fix the small axis scale (that we will now call the *resolution scale*). We want to perform wavelet analysis for ten different long axis scales (now called *integration scale*) and twenty different azimuts. This leads us to the setting up of 200 maps that we will have to compare, correlate, synthetize ... etc ... This huge quantity of data that needs to be processed is the main reason why the anisotropic wavelet transform is rarely used. Now, with the arguments developed at the end of Section 3 in mind, we propose a method to express all the information produced by an anisotropic analysis. The next section deals with a new algorithm based on filter optimization concepts: the Optimum Anisotropic Wavelet Coefficient Method.

5 The Optimum Anisotropic Wavelet Coefficient Method

The ideas and concepts described above lead us directly to our main topic, the definition of a new procedure of optimized local filtering. This procedure is the following:

(1) we choose the resolution scale (*i.e.* a);

(2) we impose the bounds of the possible integration scales (*i.e.* σa) to be used. These bounds generally correspond to the sampling scale and to the size of the signal;

(3) we make the integration scale vary by steps equal to the resolution scale, while the azimuth θ is varied from 0 to π in steps of $\frac{\pi}{36}$ (the azimut is the angle between the long axis of the wavelet and the Ox axis). A wavelet coefficient map is computed for each combination (θ,σ);

(4) we select for each point of the signal the greatest wavelet coefficient obtained in the computed maps: the *Optimum Anisotropic Wavelet Coefficient.* This gives us a kind of maximum contrast map. Moreover, each OAWC is associated with an optimum computa-

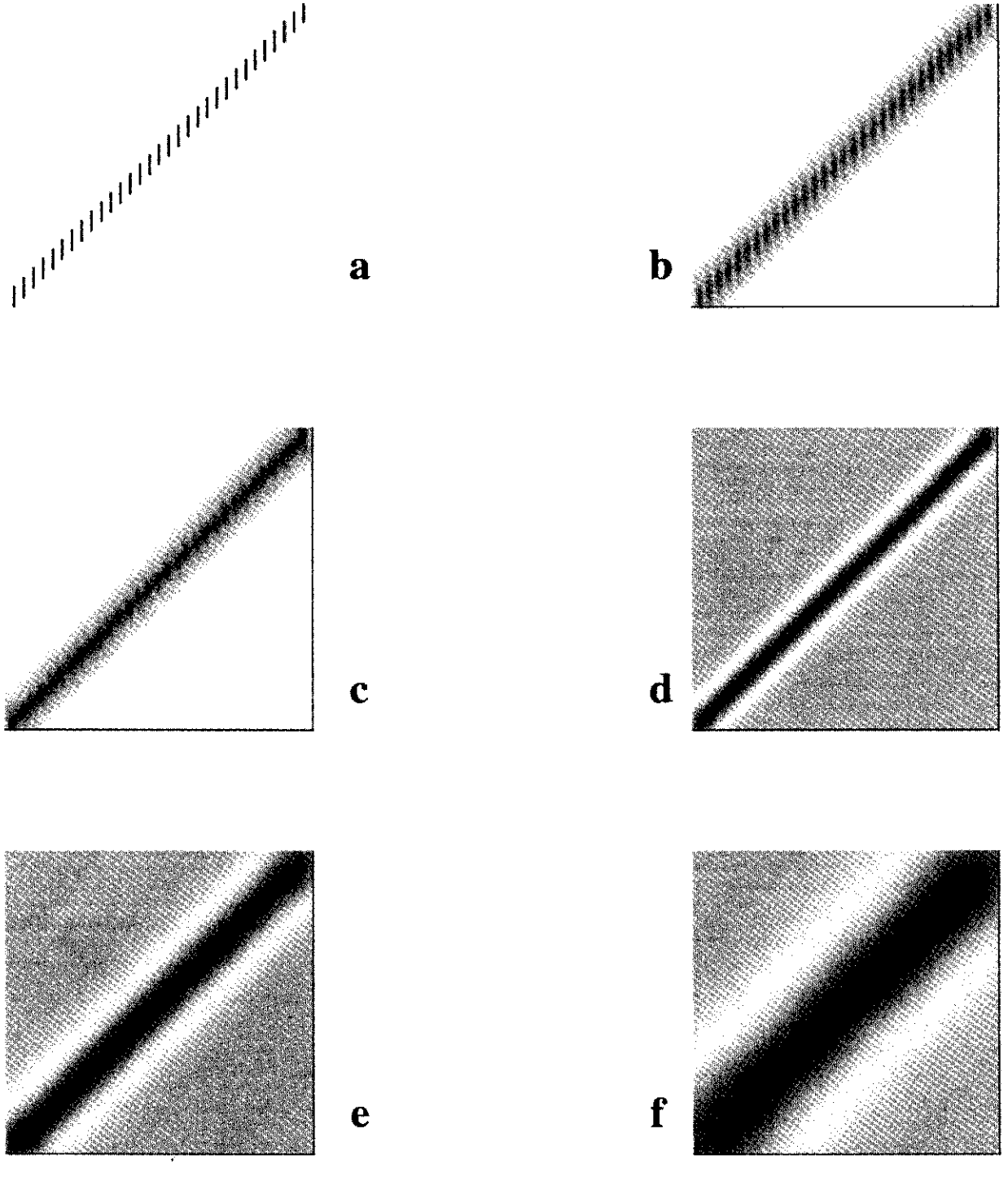

Fig. 5: Isotropic wavelet analysis of Fig. 4 (reproduced in 5a). Scales of analysis are respectivelely $a = 2(b), 4(c), 8(d), 16(e)$ and $32(f)$ pixels. Wavelet coefficients have been rescaled between 0 (white) and 1 (darkest grey).

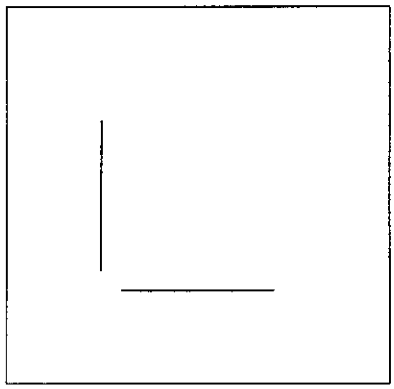

Fig. 6: Segments defining normal directions that are used for wavelet analysis presented in Fig. 7a and 7b. Each segment is 100 pixels long.

tion wavelet, whose azimuth is known. This azimuth corresponds to the orientation of the detected structure around the computation point, at the given resolution;

(5) we threshold our OAWC map in order to keep only the most significant features. We draw the crest lines of the remaining parts of the map, which we assume to correspond with the axis of the main detected structures. In the case of fault arrays, these lines could correspond to the faults we would see on a map, at a coarser resolution. We will call them *Virtual Rupture Lines*.

(6) the last step allows us to bring one of the most original contribution of this method to the description of the multiscale behaviour of signals. Indeed, we are now able to compute an histogram of the azimuths of the optimal wavelets associated to the points belonging to the VRL's. This is what geologists call *rose diagrams* when they deal with fractures. These rose diagrams then give us a general view of the anisotropy of our fields, and the variation of this anisotropy with scale. To avoid ambiguity, we specify that if a selected point is associated to an isotropic wavelet, no orientation is assigned.

Thus, we can see that this method builds an optimized summary of the signal at any given analyzing scale. The idea is that if a 'renormalized' rose diagram undergoes a sharp modification around a given scale, then this scale contains important information about the growth process of the fault pattern. When such a scale is detected, we perform new analyses, following a dichotomy principle, to determine its value with better accuracy. In principle, the method defined above can be applied to any kind of signal and the dimensionnality of the problem can also be extended (to 3D or more). However, the computation time could become a limiting factor.

6 Multifractal analysis

The concept of multifractality allows the statistical description of self-similar measures (Halsey et al, 1986), that are measures displaying scale-invariance. Consider a measure $\mu(x,y)$ distributed on a domain of linear dimension L. We cover this domain by a regular grid of mesh size ϵ and define the weight p_i of the box i as:

$$p_i(\epsilon) = \frac{\int\int_{box\ i} \mu(x,y)dxdy}{\int\int_{whole\ space} \mu(x,y)dxdy} \qquad (5)$$

i varies from 1 to $N(\epsilon)$, where $N(\epsilon)$ is the number of non-empty boxes at scale ϵ. We can define the q^{th}-order moments of the distribution p_k. These are:

$$M_q(\epsilon) = \sum_{k=1}^{N(\epsilon)} p_k(\epsilon)^q \qquad (6)$$

where q is an arbitrary real number. Then, we can define a set of *generalized fractal dimensions* D_q as:

$$D_q = lim \frac{1}{q-1} \frac{Log(M_q(\epsilon))}{Log(\epsilon)} \qquad (7)$$

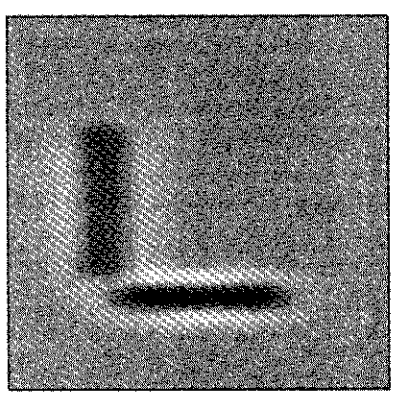

Fig. 7a: Anisotropic wavelet analysis of Fig. 6, with $a = 4$ and $\sigma = 2$. The azimuth of the wavelet is 0 such that the long axis is horizontal. Wavelet coefficients are rescaled to fit the interval between 0 (white) and 1 (darkest grey).

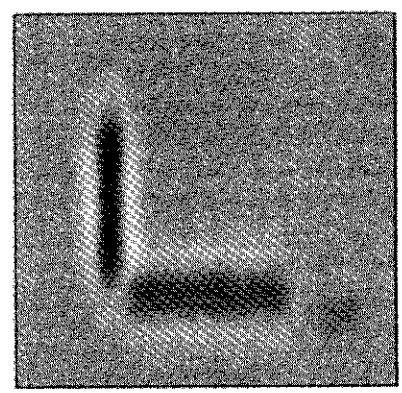

Fig. 7b: Anisotropic wavelet analysis of Fig. 6, with $a = 4$ and $\sigma = 2$. The azimuth of the wavelet is $\pi/2$ such that the long axis is vertical. Wavelet coefficients are rescaled to fit the interval between 0 (white) and 1 (darkest grey).

One can check that for $q = 0$, one recovers the *capacity dimension* of the measure, that characterizes only the geometry of the support of the measure. When $q = 1$, one obtains the *information dimension*, that expresses the rate of information we lose on the measure as we inspect it with higher resolutions. The case $q = 2$ defines the *correlation dimension*. One can show that D_q is a decreasing function of q, except when the measure is homogeneously distributed over its fractal support: D_q is then a single-valued function, equal to the fractal dimension of the support. Varying q allows one to describe the heterogeneity of the measure. For example, a large positive value of q will give information about the densest boxes. On the other hand, a high modulus but negative value of q will give information about the less dense boxes.

The next step is to define the *multifractal spectrum* of a measure. Returning to equation (5), a homogeneous fractal set is a set where the quantity $p_i(\epsilon)$ varies as ϵ^{-D_0}, where D_0 is the fractal dimension. A multifractal set is a set such that $p_i(\epsilon)$ varies as ϵ^{α}, where *alpha* is a local quantity, *i.e.* is allowed to vary from box to box and is called the *singularity strength*. A simple Legendre transform can be used to derive α and $f(\alpha)$ (that will be defined below) from the (q, D_q) pairs:

$$\alpha(q) = \frac{d}{dq}[(q-1)D_q] \qquad (8a)$$

$$f(\alpha(q)) = q\alpha(q) - (q-1)D_q \qquad (8b)$$

where $f(\alpha)$ is the capacity dimension of the set of points of singularity strength α. In fact, $f(\alpha(q))$ is the capacity dimension of the set of boxes that give the highest contribution to $M_q(\epsilon)$. The multifractal spectrum possesses several geometrical properties that can be deduced from the Legendre transform (Mandelbrot, 1989). First, the line of slope q that is tangent to the spectrum touches it at the point $(\alpha(q), f(\alpha(q)))$. For $q = 0$, one obtains $f(\alpha) = D_0$. As the slope of the spectrum vanishes and changes of sign at $q = 0$, the spectrum reaches its maximum at $(\alpha(0), D_0)$. The spectrum is thus concave. The intercept with the ordinate axis of the tangent of slope q is $(1-q)D_q$, and D_q is equal to the coordinates of the intersection point between this tangent and the line of equation $f(\alpha) = \alpha$. This yields $f(\alpha(1)) = \alpha(1) = D_1$. The spectrum is sufficient to describe a multifractal measure.

A classical multifractal analysis consists in estimating the sums (6), that will yield the D_q's through equation (7). Then, using the Legendre transform (8*a* and 8*b*), one is able to compute the whole multifractal spectrum. However, as the sums (6) are estimated only for a limited number of discrete values of q, the Legendre transform necessitates the function D_q to be interpolated as a function of q between the computed points. The derivation of $\alpha(q)$, hence of $f(\alpha(q))$, will then depend on the procedure adopted for such an interpolation. This is why we will use a method, originally proposed by Roux and Hansen (1990), that allows a direct estimation of α, without using the Legendre transform (8a). Consider the q^{th} order moment as defined in equation (6):

$$M_q(\epsilon) = \sum_{i=1}^{N(\epsilon)} p_i^q \sim \epsilon^{(q-1)D_q} \qquad (9)$$

Let $L_q(\epsilon)$ be defined by:

$$L_q(\epsilon) = \frac{\delta}{\delta q} M_q(\epsilon) = \sum_{i=1}^{N(\epsilon)} p_i(\epsilon)^q Log(p_i(\epsilon)) \qquad (10)$$

We have also, by definition:

$$L_q(\epsilon) \sim M_q(\epsilon)\frac{d}{dq}[(q-1)D_q]Log(\epsilon) \qquad (11)$$

that is:

$$L_q(\epsilon) \sim M_q(\epsilon)\alpha(q)Log(\epsilon) \qquad (12)$$

which yields:

$$\alpha(q) \sim \frac{1}{Log(\epsilon)}\frac{L_q(\epsilon)}{M_q(\epsilon)} \qquad (13)$$

Thus, through simple linear regression analyses, equation (7) gives us D_q, whereas equation (13) yields $\alpha(q)$ after computation of sum (10). Finally, equation (8b) allows to compute $f(\alpha)$.

We must realize, however, that the above development is purely theoretical. Accurate determinations of the spectrum can be obtained if the measure does not suffer lacunarity. Lacunarity is known to induce numerical instabilities for negative values of q since they focuse on sparse regions, which are the most susceptible to noise and poor statistics. Indeed, large negative q's characterize the poorest areas of the measure, that, in practice, often suffer from undersampling. This also generates spurious results, and this is the reason why we will consider only positive values of q.

There is another source of spurious results. We tested the multifractal tool on several synthetic sets of known multifractal spectrum, deterministic (like the Cantor dust) or stochastic (Lévy flights) and found values of D_q and $\alpha(q)$ within 0.05 to the theoretical values. The values of $f(\alpha)$, however, could be very far from the exactly known value. A simple error analysis of equation (8b) explains this. Using Δ to denote the error, we get:

$$\Delta(f(\alpha)) = |q|\Delta(\alpha(q)) + |q-1|\Delta(D_q) \qquad (14)$$

Assuming that $\Delta(D_q) = \Delta(\alpha(q)) = 0.05$, one obtains (for $q > 1$):

$$\Delta(f(\alpha(q))) = \frac{2q-1}{20} \qquad (15)$$

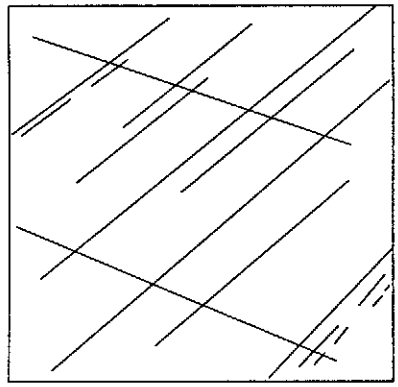

Fig. 8a: Hypothetical original network.

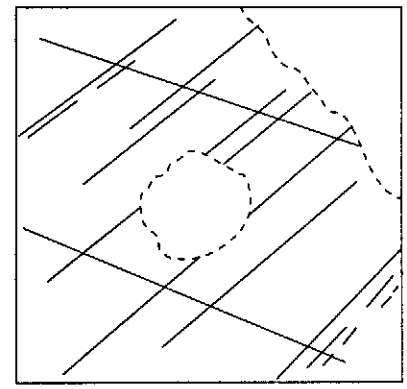

Fig. 8b: Same network as in 8a, except that some sand has deposited over it, thus creating masks that will bias the multifractal analysis.

When $q = 2$, the error is 0.15, whereas it reaches 0.65 when $q = 7$. Thus we can see that great care must be taken before computing $f(\alpha)$, even if the corresponding D_q and α are known with a high accuracy. Later in this paper, we will focus only on the values of D_q and $\alpha(q)$.

A final point concerning multifractal analysis is the influence of the finite size of the sets we have to study, as well as the influence of their irregular sampling geometry. Consider a fault system such as one of those presented in Fig. 2. The measure $\mu(x, y)$ is the Dirac function on the fault traces, and 0 anywhere else. The multifractal analysis we described can be applied but will suffer from the fact that the number of faults on a map is limited, mainly by the resolution of the original document, but also by the size of the field, whose inspection is time-consuming. As every finite size population induces biases into the statistical estimators developed to describe it, the same also holds true for the multifractal formalism. Some tests on finite-size synthetics showed that this effect was more pronounced as q increased. The measured values of D_q and α tend to be lower than the theoretical values. In the same way, if the sampling area possesses irregular boundaries, the computation is also biased. Examine Fig. 8a which represents an hypothetical fault network that is perfectly exposed. Now, imagine that some sand is deposited on the area. Fig. 8b represents the fault network that is now observable. As some faults are now hidden (at least partly) on the edges and in the center of the field, a spatial analysis will be biased. The method we propose, in the spirit of the work of Bauer et al (1993), is to compare two fault sets. The first one is the real fault network, affected by edges and finite population effects (Fig. 8b). We suppose here that we are able to define the positions and the sizes of the masks that hide some faults. The second is a random network. This network is generated as follows: we take each apparent fault of network 8*b* and place it at random. However, the faults conserve their lengths and orientations, but must avoid the masks (see Fig. 9). Thus, we argue that this new network is a random network that suffers the same censorships and finite size effects than the original one. So, if the D_q's and α's we measure on the original network equal those of the random one, we can conclude that the original one was random itself. The theoretical formalism is the following: let M_q's be the q^{th} order moments for the original network. Let M_q^* be the q^{th} order moments for the random network. We have:

$$D_q = \frac{1}{q-1}\frac{\delta Log(M_q(\epsilon))}{\delta Log(\epsilon)} \qquad (16a)$$

$$D_q^* = \frac{1}{q-1}\frac{\delta Log(M_q^*(\epsilon))}{\delta Log(\epsilon)} \qquad (16b)$$

The theoretical values of the generalized fractal dimensions of the random network are, by definition:

$$D_{q,th}^* = 2 \qquad (17)$$

The problem is now to estimate the theoretical generalized dimensions $D_{q,th}$ of the real network. Let be ϵ_{eff} such that:

$$D_{q,th}^* = \frac{1}{q-1}\frac{\delta Log(M_q^*(\epsilon_{eff}))}{\delta Log(\epsilon_{eff})} \qquad (18)$$

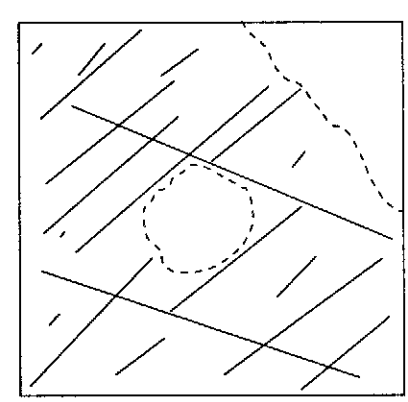

Fig. 9: Randomized version of the network presented in 8b.

Note that ϵ_{eff} can be a non-trivial function of ϵ. ϵ_{eff} introduces a kind of distorted measure that allows to suppress edge and finite size effects. So, $D_{q,th}$ must verify:

$$D_{q,th} = \frac{1}{q-1}\frac{\delta Log(M_q(\epsilon_{eff}))}{\delta Log(\epsilon_{eff})} \tag{19}$$

Together, (18) and (19) yield:

$$\frac{D_{q,th}}{D^*_{q,th}} = \frac{\delta Log(M_q(\epsilon_{eff}))}{\delta Log(M^*_q(\epsilon_{eff}))} \tag{20}$$

That is:

$$D_{q,th} = 2\frac{\delta Log(M_q(\epsilon_{eff}))}{\delta M^*_q(\epsilon_{eff})} \tag{21}$$

As now ϵ_{eff} is a dummy variable, we can replace it by ϵ:

$$D_{q,th} = 2\frac{\delta Log(M_q(\epsilon))}{\delta Log(M^*_q(\epsilon))} \tag{22}$$

Thus, a simple representation of $Log(M^*_q(\epsilon))$ versus $Log(M_q(\epsilon))$ will yield the unbiased $D_{q,th}$ of the real network. Using equation (22), one can check that if the real network is itself random, then all $D_{q,th}$'s equal 2. A similar formulation can be done for the $\alpha's$. Recently, Walsh and Watterson (1993) became aware of the problem of sampling in an irregular domain. They proposed a method that we will not detail here. Note, however, that their method does not take account of finite size effects and that it *a priori* reduces the range of scales of the analysis. On the other hand, Eneva (1994) proposes a technique close to our's to study earthquakes catalogs. However, the correction she applies to the dimensions she determines is additive whereas our correction is multiplicative and theoretically founded.

Of course, scaling relationships will often be valid only in a limited range of scales (see Fig. 10). In our study, the largest one will always be the size of the studied map and is not of interest. On the other hand, we argue that the small one is of primary importance, as it defines a physical boundary of a certain kind of behaviour. It will then be considered as a characteristic scale that affects the growth of our fault pattern. However, one could argue that this inner scale is simply due to the finite resolution of sampling. We have therefore checked with the multifractal analysis as well as the wavelet analysis for each map, that the detected transition scales are always greater than the resolution of that map.

7 Multiscale analysis of the data

The aim of this paper is to show that we are able to detect and characterize transition scales that exist in the fracturing of a continental plate. This can be done by coupling the wavelet and multifractal analysis. First, we

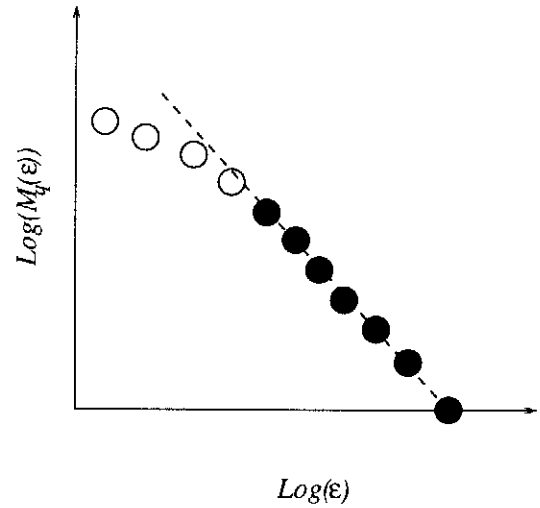

Fig. 10: Typical behaviour of $M_q(\epsilon)$ in a $Log - Log$ plot. Black circles represent points that belong to the scaling regime. The scale limit between white and black circles defines an inner scale that can be interpreted as a characteristic scale for the physics of the system under study.

check that this method is relevant by testing it on the synthetic example of *en échelons fractures*, as defined in Section 3. Fig. 11 represents an OAWC analysis of Fig. 4 at resolutions of 2 and 4 pixels. At scale 2 pixels, the Virtual Rupture Lines mimic perfectly the original network, as do the rose diagram. At the 4 pixels scale, there is only one VRL left, that strikes N45E, as does now the rose diagram. Thus, our wavelet method works, allowing us to recover macroscopic properties from microscopic ones. A multifractal analysis was performed on the same data set. We present results only for D_0 (Fig. 12). At both large and small scales $D_0 = 1$, but the existence of a transition scale between both regimes can be clearly observed. Note that this scale is identical to the scale at which we observed a rotation with the OAWC analysis. Thus, while a multifractal analysis allows to detect the existence of a transition scale, the wavelet analysis allows us to characterize it by the existence of a possible rotation of the structures. This example is trivial, but, when applied to more complex networks, the analysis yields useful results. It is possible that transitions scales will be detected by one method and not by the other. As a fracture network seems to be characterized by two main parameters (*i.e* local density and orientation), our method should be able to detect these main characteristic scales.

We now present our results obtained on real fault networks in Fig. 2. Map III was not studied in its entirety (see Fig. 13a). We selected the northeastern corner, to avoid the influence of the sand-filled graben striking N135E which hides some faults. This is done because, in contrast to the multifractal analysis, the wavelet analysis is unable to take account of such a bias. In the selected domain, at this scale, the probability

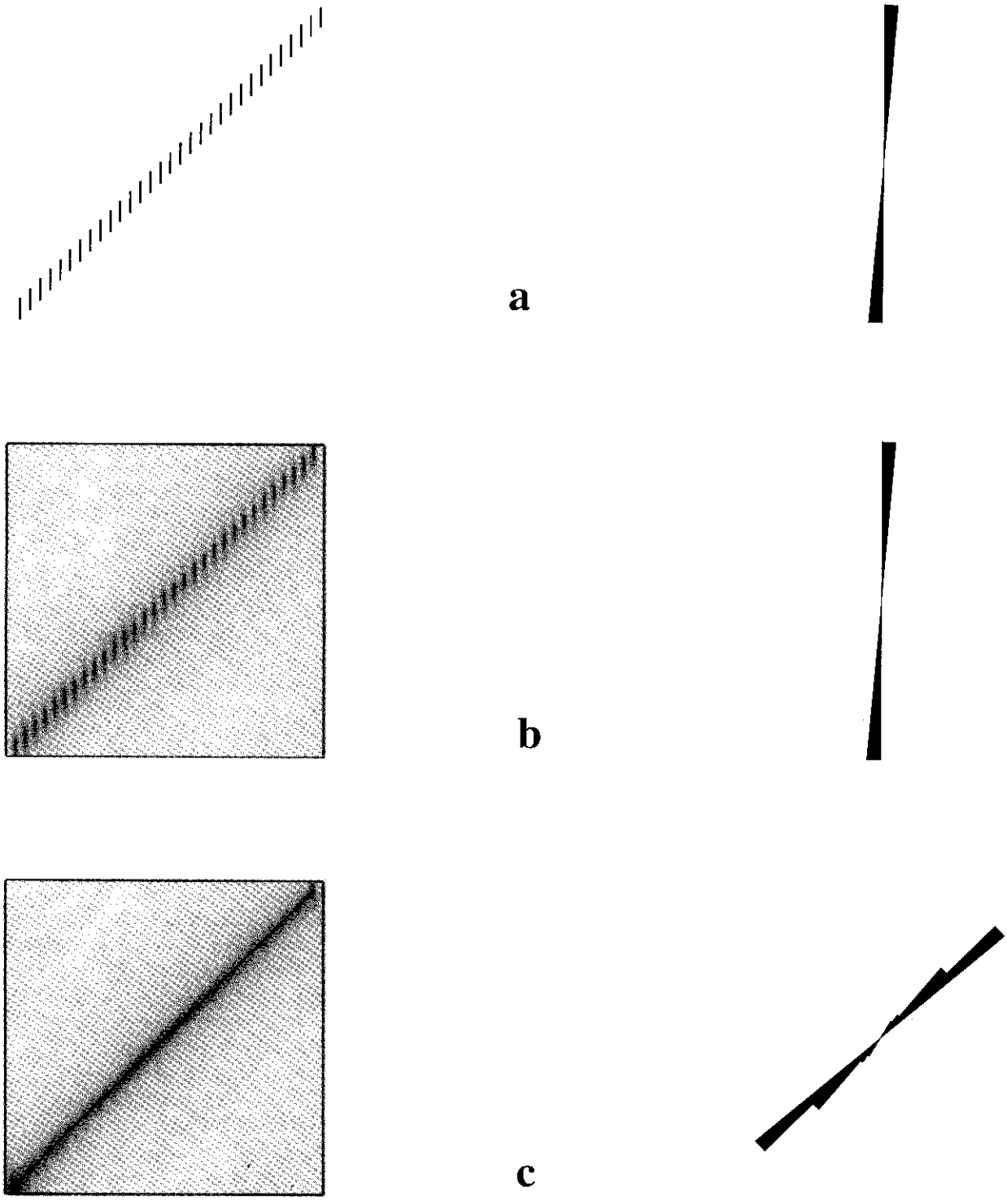

Fig. 11: OAWC analysis of Fig. 4. Case a represents the original signal with its 'microscopical' rose diagram on its right. Cases b and c stand for analyses at scales of 2 and 4 pixels repectively. Case b reveals no change when compared to case a. On the contrary, case c shows a sharp rotation of the structure, as revealed by the rose diagram. The transition scale detected here is 4x2.2 9 pixels. Virtual Rupture Lines are drawn in black, whereas wavelet coefficients have been rescaled between 0 (white) and 1 (darkest grey).

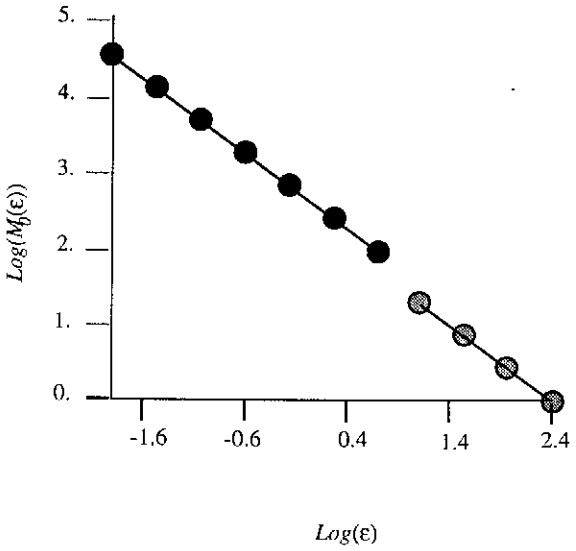

Fig. 12: Box-counting multifractal analysis of Fig. 4 for $q = 0$. ϵ is given in pixels, to allow comparisons with Fig. 11. The large-scale regime (grey circles) gives a slope of -1, Thus $D_0 = 1$. The small-scale regime (black circles) also yields $D_0 = 1$. However, one can note a small 'jump' between both regimes, at a scale slightly greater than 8 pixels. This scale correlates very well with the one discovered in Fig. 11.

to find a similar graben is quite low. We thus argue that the northeastern corner is more representative of the fracture regime of the Arabian Plate at the scale of 1 : 62,500 than is the whole map. In the same way, Map II was studied only in the square which is shown in Fig. 13b, located in the middle of Map II. Finally, Map VI was not analyzed directly but will serve as a reference to illustrate the usefulness and power of our wavelet analysis on real data. In order to avoid to overlengthen this paper, all figures concerning multifractal exponents determination and anisotropy changes were not reproduced here but are available in Ouillon (1995).

Map I: this map is concerned with jointing. Both wavelet and multifractal analyses gave a transition scale of about 1 to $1.5m$. The multifractal analysis also showed that above this scale, D_q's as well as α's are equal to 2, *i.e.* fracturing is a spatially homogeneous process. Below this scale, and down to $1cm$, the structure seems more complex (see Fig. 2) but cannot be described by a self-similar behaviour.

Map II: here again, we analyse jointing. The transition scales we obtained are very close to the one obtained in Map I (about $1.6m$ (multifractal) and $1.8m$ (wavelet)). Above this scale, all the critical exponents equal 2.

Map III: the structures we see now are faults. All the critical exponents are still equal to 2, down to the characteristic scale of $600m$. Fig. 14a shows a comparison between exponents obtained with a classical multifractal analysis and exponents obtained with our de-biasing analysis. As one can see, without 'de-biasing', one would

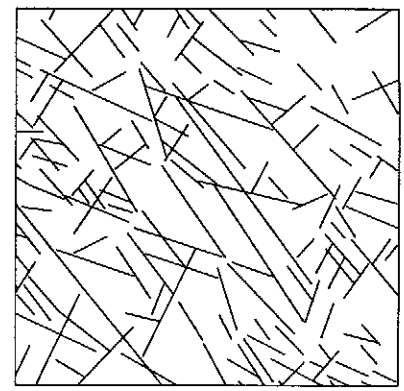

Fig. 13a: Part of Map III that was retained for analysis (see text). It fits with the northeastern corner of Map III. Its linear size is $5,500m$.

have wrongly concluded the existence of multifractality. Note that the wavelet analysis reveals a transition scale of $700m$.

Map IV: here again, we are dealing with faults. The wavelet analysis reveals a scale of $6.5km$. The multifractal analysis yields a scale of $6km$, but now the critical exponents are decreasing functions of q. We thus have evidence of multifractality, that is heterogeneity in the fracture regime. It is interesting to note that $D_0 = 2$, whereas D_q and $\alpha(q)$ seem to tend to 1.75 when q tends towards large values.

Map V: this map is also concerned with faulting. Fig. 15 shows the results of the OAWC analysis at resolutions of 2, 4, 8, 16 and 32 pixels. This yields two transition scales: $21km$ and $43km$. The multifractal analysis yields a third scale of $12km$. Above this scale, we observe multifractality. We still have $D_0 = 2$, whereas now D_q and $\alpha(q)$ seem to tend to 1.75 when q gets large. Fig 14b allows the comparison between biased and unbiased determinations of $\alpha(q)$.

Figure 16 presents an interpretation of the area covered by Map V using a satellite picture at the 1 :

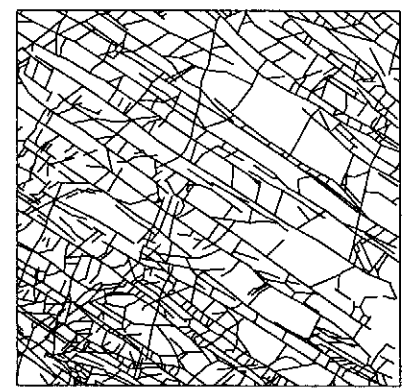

Fig. 13b: Part of Map II that was used for analysis. It fits with the central part of Map II. Its linear size is $25.8m$.

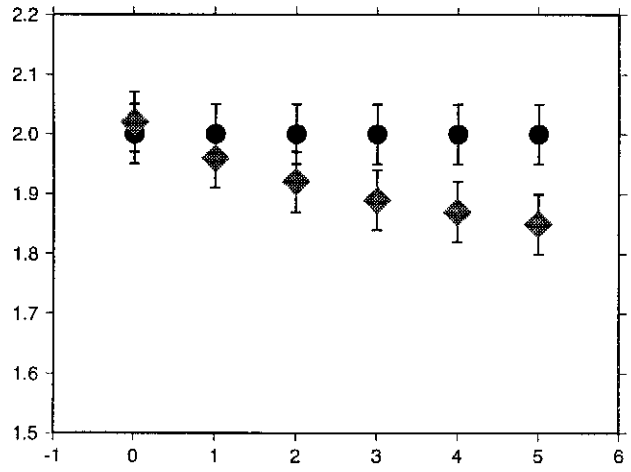

Fig. 14a: α values as a function of q for Map III. Circles are for exponents corrected for sampling effects, squares for uncorrected ones. In the uncorrected case, α varies with q, thus suggesting some multifractality. Correction for sampling bias reveals that α is constant with q, thus that the set is homogeneous. The figure, for the sake of clarity, deals only with a limited range of q's.

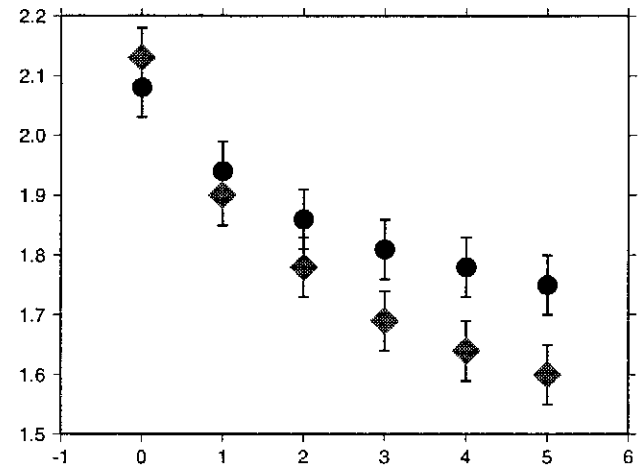

Fig. 14b: α values as a function of q for Map V. Circles are for exponents corrected for sampling effects, squares for uncorrected ones. Even after correction, α is not constant with q, leading to the conclusion that the set displays some genuine multifractality.

1,000,000 scale (that is the zone located in the dashed frame in Map VI). As Map V was initially at the 1 : 250,000 scale, a 2 pixels analysis should be equivalent to the satellite imagery. VRL's determined at 2 pixels (see Fig. 15, case b, but also presented on Fig. 16) are in good agreement with faults of the top of Fig. 16. We can also note the good agreement between both rose diagrams. This shows that the OAWC method offers a reliable and objective tool to analyze complex fault patterns at different scales.

A geological interpretation of this quantitative analysis will be presented in Section 9.

8 Frequency-length analysis of fault traces

A complementary analysis of the data was performed using a frequency-length analysis of fault traces. It consists simply in estimating histograms relating a fault length l to the number of faults with lengths comprised between l and $l+dl$, denoted $N(l)dl$. Fig. 17 shows histograms corresponding to maps II to V, in a $Log - Log$ representation. Map I was not analysed because of censorship effects (most of the fractures cut the edges of the field) inducing bias. A linear fit was performed on each data set to estimate the slope of the lines. Note that the existence of a linear relationship implies the existence of a power law for $N(l)$, that is scale invariance:

$$N(l)dl \sim l^{-(c+1)}dl \qquad (23)$$

c was found equal to 0.9 for Map II, 1.1 for Map III and 1.1 for Map V. For Map IV, c was found equal to 2.2. However, when inspecting Map IV, we can note that this map represents a complex fault pattern with numerous faults that intersect and offset each other. Thus, the digitization of the map may have caused more small faults to be identified than actually exist, hence increasing c. We can also note that the power law seems to hold (with a constant exponent) up to a scale of about $12km$, which can be compared with the characteristic scale discovered in Map V using the multifractal analysis. Above a length of $12km$, there is a strong deviation from the initial power law. Due to the lack of data, it is not possible to determine the nature of this large scale distribution: is it still a power law (with a c-value somewhat larger than 1) or another type of behaviour ? An exponential fit was also performed on the data set of Map V (considering lengths greater than the resolution of the map). The 'relaxation' length that appeared in the exponential was of the order of $3km$. However, we do not consider that this solution is statistically valid, since only a few faults have a length lower than $3km$ on this map. Note that our small-scale c value ($\simeq 1$) is in good agreement with the work of other authors (Scholz and Cowie, 1990; Gudmunsson, 1987; Villemin et Sunwoo, 1987; Sornette et al, 1993; Sornette and Davy, 1991).

Finally, we would like to mention the implication of a power-law distribution for our previously detected transition scales. A power-law implies that the number of faults should diverge for short lengths (equation (23)). As can be observed in Fig. 17, for each map, there always exists a typical length below which the number of faults starts to decrease. We believe that it is a sampling effect: this underlines the resolution scale of the map, below which all the faults are no longer detected. This is why we did not consider transition scales that were found on maps that present a larger detection threshold (see Sections 6 and 7).

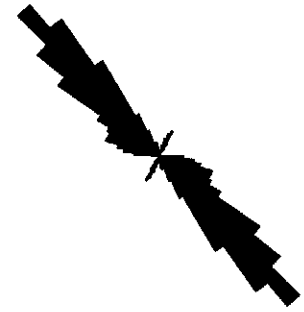

a

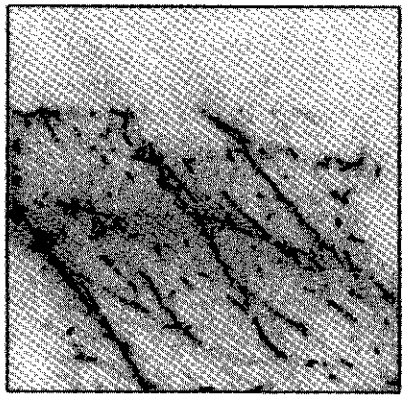

b

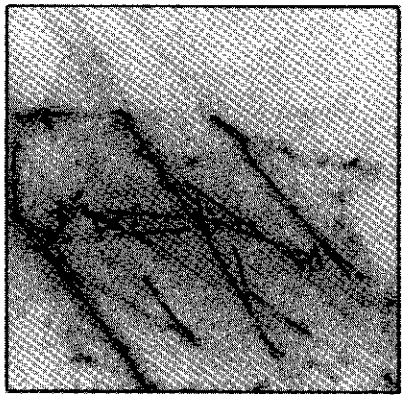

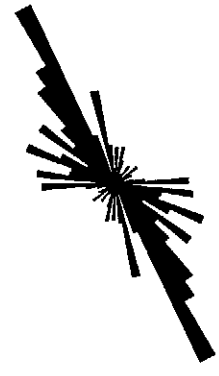

c

Fig. 15: OAWC method applied to Map V. The original picture is shown in case a. Wavelet coefficients are rescaled between 0 (white) and 1 (darkest grey). Black dots represent the VRL's. Rose diagrams on the right are associated either with the original pattern or the VRL's (from b to f). Scales of analysis are respectively 2(b), 4(c), 8(d), 16(e) and 32 (f) pixels.

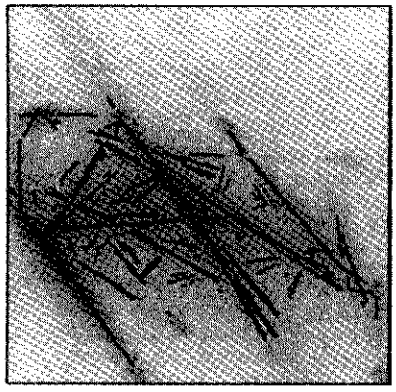

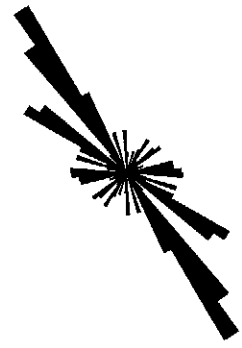

d

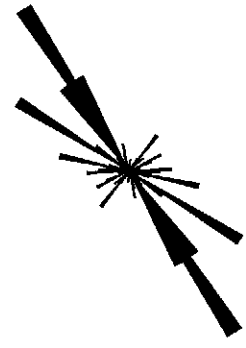

e

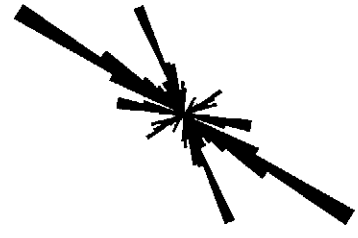

f

Fig. 15 (continued): A first transition occurs at $2.2a = 4.4$ pixels, and thus constitutes an upper bound for an undefined scale. A second transition occurs between $2.2a = 35.2$ pixels and $2.2a = 70.4$ pixels. A more detailed analysis in this range points the transition at $2.2a = 37.4$ pixels, that is $21km$.

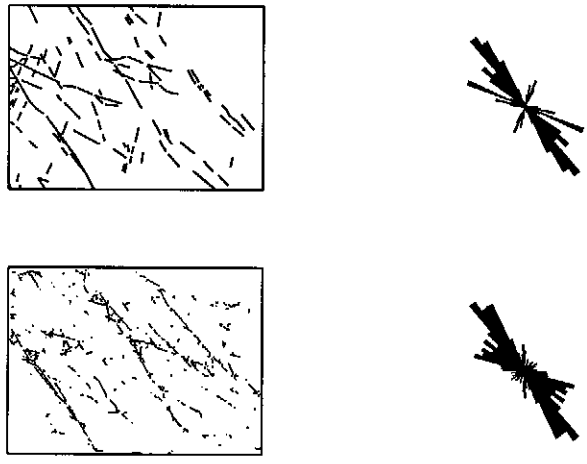

Fig. 16: Hand-drawing interpretation (top) of a satellite image at the 1 : 1,000,000 scale. This area is the same as the one contained within the dashed frame in Fig. 2, Map VI. It should be compared to the VRL's map (bottom) of Fig. 15b. Note also the good agreement between the two rose diagrams.

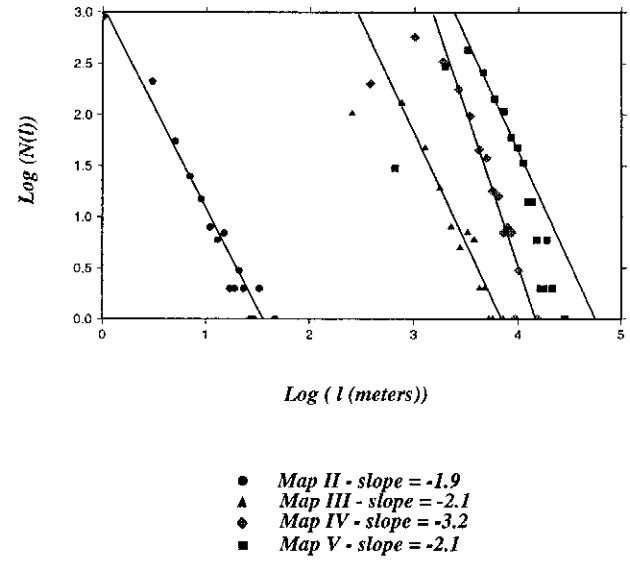

Fig. 17: Density ditribution of fault lengths for Map II to V. The scale is logarithmic for both axes. Horizontal axis is for fault length (in meters), while vertical axis is for the number of faults. Legend gives the slope of the solid lines obtained with least-squares data fiting.

9 Discussion

The previous analyses have provided the following informations about the multiscale organization of the fracturing process:

(i) *small scale fracturing* ($1m$-$6km$): all critical exponents are equal to 2, thus reflecting a spatial homogeneity of the fracturing process. Several transition scales can be found: $1m, 600m, 6km$. The exponent of fault length distribution is close to 1.0.

(ii) *intermediate scale fracturing* ($6km$-$12km$): fracturing is not homogeneous. Multifractality appears with asymptotic values of D_q and α that are close to 1.75, whereas D_0 is still 2.0. There are no intermediate scales, and the fault length distribution exponent is still close to 1.0.

(iii) *large scale fracturing* ($12km$-$100km$): multifractality holds with asymptotic exponents close to 1.75. Transitions occur at scales of $21km$ and $43km$. It is not possible to fit the fault length distribution with the same power law as before. If a power law still holds at lengths greater than $12km$, then c must be significantly larger than 1.

These results can be explained by considering structural data concerning the Arabian Plate crust. Field evidence shows that the Saq Sandstone beds are only 1 to $2m$ thick. Drilling in the sedimentary cover showed the thickness of the total Saq Sandstone formation to be roughly $600m$ (Janjou et al, geological map in preparation; Vaslet et al, 1994). Estimates suggest a total sedimentary basin thickness of about $5km$ before erosion (Janjou et al, geological map in preparation; Vaslet et al, 1994). All those thicknesses correlate well with the transition scales discovered in Section 7. Two other scales can be understood when considering the thermal layering of a typical continental crust (Carter and Tsenn, 1987). We have used Mercier's continental geotherm (Mercier, 1980) to estimate the depth/temperature profile in the Arabian crust, assuming that it is composed of granite. We checked that Mercier's geotherm was compatible with previous heat flow measurements on the Arabian Plate (Gettings et al, 1986; Pollack et al, 1993). The result is presented in Fig. 18. Two estimates are of crucial importance. First, the onset of quartz plasticity: below a temperature of $300°C$ (Scholz, 1990; Sibson, 1986; Tullis and Yund, 1977), the mechanical behaviour of quartz is *brittle*, so it behaves elastically until it reaches its rupture threshold. Above this temperature, it is *plastic*, *i.e.* it starts to flow. Second, the onset of feldspar plasticity. The brittle/plastic transition temperature is $450°C$ (Scholz, 1990; Sibson, 1986; Tullis and Yund, 1977). Inspecting Fig. 18, it can be seen that depths corresponding to both critical temperatures are respectively $11km$ and $21km$ (close to the characteristic scales of 12 and $21km$ previously determined in Sections 7 and 8). Finally, seismic experiment interpretations (Mooney et al, 1985; Prodehl, 1985; Gettings et al, 1986; Badri, 1991; Mechie et al, 1986) as well as seismological observations (Niazi, 1968; Knopoff and Fouda, 1975; Mokhtar and Al-Saeed, 1994) give a Mohorovicic discontinuity depth (that is the boundary between the crust and the mantle) between 35 and $45km$. However, the most recent results seem to favor a Moho depth slightly greater than $40km$. This fits with our last characteristic scale. Using the same data, the depth of the Conrad discontinuity (that marks the transition between the upper and lower crust) was found to be $19 - 21km$. From

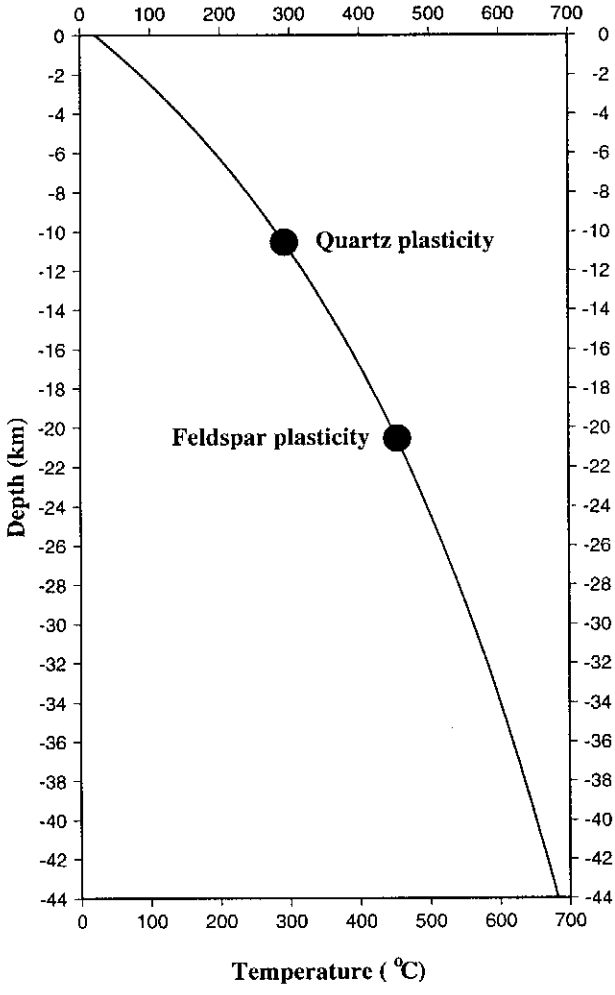

Fig. 18: Depth/temperature profile (solid line) expected in the Saudi Arabian crust from Mercier's geotherm. Full circles show onsets of plasticity for quartz and feldspar.

a rheological point of view, the Mohorovicic discontinuity can mark an abrupt change of behaviour. Below it, materials can be much stronger (Carter and Tsenn, 1987; Ranalli, 1987; Wilks and Carter, 1990; Chen and Molnar, 1983), due to a change of rock type (the dominant mineral species is olivine). Such a contrast depends on many parameters, like temperature and strain rate (Kirby and Kronenberg, 1987; Ord and Hobbs, 1989; Ranalli, 1987), and so remains uncertain in our case.

Thus, we have shown that fracturing of a continental plate is not a self-similar process from the centimeter scale up to the 100 kilometer scale. Several characteristic scales exist, that correlate very well with the thicknesses of the structural units that constitute the crust. Such a dependence was known for jointing, where it has been observed for a long time that spacing between joints in a sedimentary layer is of the order of the layer thickness (Pollard and Aydin, 1988; Narr and Suppe, 1991). It seems that our results generalize this observation to the multiscale rheological constitution of the continental crust. Note that the tabular structure of the Arabian Plate is a particularly favorable situation for providing good data sets that allow the quantitative analysis presented here.

We have now to provide an explanation to the multiscale behaviour of the critical exponents D_q, $\alpha(q)$ or c.

(i) *small scale fracturing*: in this range, the mechanical behaviour of rocks can be considered as brittle. Several experiments and models propose a proportionality relationship between fracture spacing and thickness of the fractured layer (Groisman and Kaplan, 1994; Merzer and Freund, 1976).Thus, as proposed by Banerdt and Sammis (1992), a concept of 'stress shadowing' can be adopted: Pollard and Segall (1987) have shown that, in an elastic medium, a crack submitted to a tensile stress normal to its plane was relaxing stress up to a distance comparable to the smallest dimension of the crack. This prevents other cracks from nucleation near the preexisting crack, thus defining a kind of Elementary Volume that is preserved from further fracturing. As all the EV's have the same characteristic size H (that is the thickness of the layer), fractures are equally spaced, thus inducing the existence of a characteristic scale in the horizontal plane, in the direction normal to the fracture planes, as well as a homogeneous pattern with all multifractal exponents equal to 2. However, in the horizontal plane, in the direction parallel to the fracture planes, no characteristic scale is present, thus providing favorable conditions to the existence of a self-similar behaviour of the fault length distribution, which is a power law, with an exponent c close to 1 but whose precise value remains unexplained (see however Sornette and Davy, 1991).

(ii) *intermediate scale fracturing*: our considerations on the thermal properties of the crust cause us to conclude that the layers involved in this regime are characterized by brittle behaviour. This explains the existence of a characteristic scale, as well as a c exponent that does not change, and thus seems universal. The value $D_0 = 2$ reveals the fact that each EV is broken. The fact that multifractality appears implies that fracturing is heterogeneous, that is some EV's are highly fractured, whereas others are not, and that their relative spatial locations are not random. Thus, some EV's seem to accumulate brittle strain, screening other EV's at the same time. The local structure of the most fractured EV's can be inferred through the asymptotic value of $\alpha(q)$. This value is close to 1.75, which is similar to the fractal dimension of *Diffusion-Limited Aggregation (DLA)* growth processes (Witten and Sander, 1981; Arnéodo et al, 1992). This point is discussed later.

(iii) *large scale fracturing*: two different rheological behaviours hold: between 12 and $22km$, it is *semi-brittle* (that is quartz is flowing, while feldspar is brittle); between 12 and $43km$, it is fully plastic. It seems that arguments about elastic stress relaxation around a fault

(see above) still hold, because of the existence of characteristic scales. However, a power law with c close to 1 does not seem to hold anymore. The disappearence of this power law correlates very well with the change in rheological behaviour ($12km$), thus indicating that $c = 1$ should be valid only in the brittle regime. When reaching a length of $12km$, a fault thus changes its mode of growth. In fact, as a fault grows in a more ductile medium, part of the enhanced stress at the fault tip can be partly relaxed by plastic flow (mainly accomodated by dislocation glide and climb), thus blunting the fault tip (Lawn, 1993). This ultimately leads to a reduction of the stress concentration at the fault tip, that tends to inhibate further growth. Thus, fault growth speed diminishes, resulting in higher values for c, if a power law still governs fault length distribution above $12km$. Another explanation would be that a majority of fault segments stop growing when they reach a critical size of $12km$, because they link with neighbouring segments. This is perhaps the case for the three main grabens of Map V, striking N135E, that seem to be composed of an agglomeration of smaller segments. Thus, the $12km$ scale could reflect the fact that fault growth mode changes into a linkage mode, in the spirit of percolation processes. Concerning the multifractal exponents, they are almost the same as those in intermediate scale fracturing. We can then deduce that c does not control the generalized dimensions of the fault patterns. They must be controlled by the distribution of fault barycenters (Sornette et al, 1993). The asymptotic value of $\alpha(q)$ is about 1.75.

The fracture regime is very different when we consider either the sedimentary basin or the crystalline basement. It must be pointed out that this duality seems to concern fracturing at every scale. Our study shows that jointing and faulting in the sedimentary basin are spatially homogeneous processes. It also shows that faulting in the crystalline basement seems to be a heterogeneous process. Some data concerning jointing in crystalline rocks indicate that it is generally heterogeneous (Pollard and Aydin, 1988; Martel, 1990; see also Fig. 2 and 3 in Segall and Pollard, 1983), even if this heterogeneity has still not been fully quantified. However, one of us (Ouillon, 1995) finds a fractal dimension D_0 of 1.45 for joints affecting a granitic outcrop in Saudi Arabia. The scaling behaviour seems to be valid from the centimeter scale (the size of the mineral crystals) up to the scale of the outcrop size ($600m$)(those results will be presented with more details elsewhere). Thus, fracturing of the crystalline material seems to be heterogeneous even at small scales. A question then naturally arises: why is fracturing of the crystalline crust heterogeneous whereas it is homogeneous in the sedimentary basin ? We believe that the answer has to be found into the mechanical coupling conditions within the different units. Some detachment planes can exist at the base of the sedimentary basin, and within the basin itself (clay horizons, or weak interfaces between beds, for instance). Then, the basin reacts as a pile of elastic beds separated by potential detachment planes, leading to the development of a hierarchical fracture network: each unit develops its own pattern, at every scale we can consider, following the stress shadowing principle. On the other hand, in the crystalline crust, the three main layers are bound together, so that the coupling is strong (note, however, that the existence of characteristic scales in the crystalline crust can also reveal the existence of potential detachment planes (see below)). Thus, deformation is a competition between the localizing properties of brittle deformation, and diffusion properties of the plastic flow process. Note that it has been argued (Sornette (1990) for instance) that this competition is analogous to a Diffusion-Limited Aggregation growth process, generating self-similar structures (Witten and Sander, 1981; Arnéodo et al, 1992). As quoted before, we should note that recent developments in the study of the rheology of the crust lead to the possible existence of more or less well-defined detachment zones within the crust (Ord and Hobbs, 1989). The depths at which such detachments occur depend strongly on the composition of the crust, the geothermal gradient, the tectonic environment as well as the imposed strain rate. Thus, more detailed investigations are needed to eventually correlate our crustal characteristic scales with some possible detachment zones. In addition, other recent results suggest that the fault network organization may be even more complicated. Numerical simulations of fault growth by repeated earthquakes (Miltenberger et al, 1993) showed that 2D fault growth is highly controlled by the preexisting horizontal mechanical heterogeneity. This confirmed observations of crack propagation in granite (Gentier, 1987) that showed that crack paths are not random but correlated with the position of rock-constitutive minerals, which in turn are not randomly located because of chemical thermodynamical affinities or incompatibilities between mineral species. Finally, even in the crystalline rocks, our study reveals that horizontal layering of the crust also controls the morphology of the fault pattern. Thus, complex patterns of faulting could also be, in part, the result of a competition between horizontal disorder and vertical structure of the crust.

To end this dicussion, we should point out that similar results have been found by other workers. Hatton et al (1994) studied the length-displacement relationship of tensile fractures in the Krafla fissure swarm (NE Iceland). Their data display about four orders of magnitude in length and five orders in displacement. They observe that two power-laws hold in different scaling ranges. They correlate the cutoff scale ($3m$) with the spacing of pre-existing cooling joints that shield stress at a small scale, preventing small crack stress to be transfered to distant mechanical grains (that are about $30cm$

in size). A crustal-scale analysis was conducted by Davy (1993) on the San Andreas fault system. Davy computed the fault length distribution of the network and proposed a fit using a gamma law. This law behaves at small scales as a power-law (yielding a c exponent of 1.3). At large scales, the function behaves as an exponential, with a characteristic length of $24km$. This scale is then correlated with the thickness of the brittle crust in California, inferred from the depth distribution of earthquakes. However, we must note that it is still a matter of debate whether the maximum depth of earthquakes is controlled by the brittle-ductile mechanical transition (Sibson, 1986; Tullis and Yund, 1977), or by the transition of slip-weakening to slip-strengthening friction regimes (Scholz, 1990; Ord and Hobbs, 1989).

10 Conclusions

The aim of this paper was first to introduce a new method of filtering coined the Optimal Anisotropic Wavelet Coefficient method, as a useful tool for studying multiscale behaviour. We have shown that this method can give information about the anisotropic properties at every scale. We used this method, as well as a new multifractal analysis tailored to correct for edge or finite size effects, to study the multiscale behaviour of several fracture networks mapped in Saudi Arabia. The main result of our work is that fracturing of a continental plate is not a self-similar process from the centimeter scale up to the one hundred kilometer scale. Spatial distribution of joints and faults appears to be controlled by the thicknesses of the different rheological beds that constitute the crust. From the centimeter scale up to the sedimentary basin scale, fracturing is a spatially homogeneous process, although displaying scale invariance in the fault length distribution, with an exponent that seems universal when dealing with brittle deformation processes. At larger scales, concerned with the granitic basement, multifractality holds. Even if fractures seem distributed everywhere ($D_0 = 2$), faulting displays local singularity strengths that are close to the one observed in homogeneous Diffusion-Limited Aggregation growth processes (of fractal dimension 1.7). This feature could be the result of the subtle competition and coupling between the brittle behaviour of the upper crust, the semi-brittle behaviour of the intermediate crust, and the plastic behaviour of the lower crust. Brittleness tends to localize deformation whereas ductile flow tends to homogenize it. However, more work is needed to explain the values of the critical exponents.

Acknowledgements. The authors would like to thank the field staff of B.R.G.M. for data acquisition and interpretation. We would also like to thank Alain Arnéodo, Christophe Larroque, Anne Sornette, Marc Sosson, Christian Vanneste and Jean Virieux for discussions on geological, mathematical, numerical or physical aspects of this work. This work is supported by B.R.G.M.

References

Antoine, J.P., Murenzi, R., Piette, B., Duval-Destin, M.; Image analysis with 2D continuous wavelet transform: detection of position, orientation and visual contrast of simple objects, in *Wavelets and Applications*, Y. Meyer Editor, Masson, 1992

Arnéodo, A., Argoul, F., Bacry, E., Elezgaray, J., Freysz, E., Grasseau, G., Muzy, J.F., Pouligny,B.; Wavelet transform of fractals, in *Wavelets and Applications*, Y. Meyer Editor, Masson, 1992

Badri, M.; Crustal structure of central Saudi Arabia determined from seismic refraction profiling, *Tectonophysics, 185*, 357-374, 1991

Banerdt, W.B., Sammis, C.G.; Small-scale fracture patterns on the volcanic plains of Venus, *J. Geophys. res., 97*, E10, 16149-16166, 1992

Bauer, M., Heng, H., Martienssen, W.; Characterization of spatiotemporal chaos from time series, *Phys. Rev. Lett., 71*, 521-524, 1993

Carter, N.L., Tsenn, M.C.; Flow properties of continental lithosphere, *Tectonophysics, 136*, 27-63,1987

Chandler, D.; *Introduction to Modern Statistical Mechanics*, Oxford University Press, 1987

Chen, W.P., Molnar, P.; Focal depths of intraplaque earthquakes and their implications for the thermal and mechanical properties of the lithosphere, *J. Geophys. res., 88*, B5, 4183-4214, 1983

Davy, P.; On the frequency-length distribution of the San Andreas fault system, *J. Geophys. Res., 98*, B7, 12141-12151, 1993

Diu, B., Guthmann, C., Lederer, D., Roulet, B.; *Physique Statistique*, Hermann, 1989

Eneva, M.; Monofractal or multifractal: a case study of spatial distribution of mining induced seismic activity, *Nonlin. Proc. in Geophys., 1*, 182-190, 1994

Freund, R., Garfunkel, Z., Zak, I., Goldberg, M., Weissbrod, T., Derin, B.; The shear along the dead Sea rift, *Philos. Trans. R. Soc. London, Ser. A, 267*, 107-130, 1970

Gentier, S.; *Morphologie et Comportement Hydromécanique d'une Fracture Naturelle dans le Granite sous Contrainte Normale - Etude Expérimentale et Théorique*, Documents du BRGM, 134, Editions du BRGM, 1987

Gettings, M.E., Blank, H.R. Jr., Mooney, W.D., Healey, J.H.; Crustal structure of Southwestern Saudi Arabia, *J. Geophys. Res., 91*, B6, 6491-6512, 1986

Giannérini, G., Campredon, R., Féraud, G., Abou Zakhem, B.; Déformations intraplaques et volcanisme associé: exemple de la bordure Nord-Ouest de la plaque Arabique au Cénozoique, *Bull. Soc. Geol. France, (8), t. 4*, 6, pp. 937-947, 1988

Groisman, A., Kaplan, E.; An experimental study of cracking induced by desiccation, *Europhys. Lett., 25*, 6, 415-420, 1994

Grossmann, A., Morlet, J.; Decomposition of Hardy functions into square integrable wavelets of constant shape, *SIAM J. Math. Anal., 15*, 723-736, 1984

Gudmunsson, A.; Tectonics of the Thingvellir fissure swarm, SW Iceland, *J. Struct. Geol., 9*, 61-69, 1987

Halsey, T.C., Jensen, M.H., Kadanoff, L.P., Procaccia, I, Shraiman, B.I.; Fractal measures and their singularities: the characterization of strange sets, *Phys. Rev. A, 33*, 1141-1151, 1986

Hatton, C.G., Main, I.G., Meredith, P.G.; Non-universal scaling of fracture length and opening displacement, *Nature, 367*, 160-162, 1994

Herrmann, H.J., Roux, S. (Editors); *Statistical Models for the Fracture of Disordered Media*, North-Holland, 1990

Husseini, M.I.; Tectonic and deposition model of late precambrian-cambrian Arabian and adjoining plates, *A.A.P.G. Bull., 73*, 1117-1131, 1989

Kagan, K.K.; Fractal Dimension of brittle fracture, *J. Nonlinear Sci., 1*, 1-16, 1991

Kirby, S.H., Kronenberg, A.K.; Rheology of the lithosphere: selected topics, *Rev. Geophys., 25*, 6, 1219-1244, 1987

Knopoff, L., Fouda, A.A.; Upper-mantle structure under the Arabian peninsula, *Tectonophysics, 26*, 121-134, 1975

Lawn, B.; *Fracture of brittle solids*, second edition, Cambridge University Press, 1993

Mandelbrot, B.B.; Multifractal measures, especially for the geophysicist, in *Fractals in Geophysics*, C.H. Scholz and B.B. Mandelbrot Editors, Birkhauser Verlag, 1989

Mandelbrot, B.B., Passoja, D.E., Paullay, A.J.; Fractal character of fracture surfaces of metals, *Nature, 308*, 721-722, 1984

Martel, S.J.; Formation of coumpound strike-slip fault zones, Mount Abbot quadrangle,California, *J. Struct. Geol., 12*, 7, 869-882, 1990

Mechie, J., Prodehl, C., Koptschalitsch, G.; Ray path interpretation of the crustal structure beneath Saudi Arabia, *Tectonophysics, 131*, 333-352, 1986

Mercier, J.-C.C.; Single-pyroxene thermobarometry, *Tectonophysics, 70*, 1-37, 1980

Merzer, A.M., Freund, R.; Equal spacing of strike-slip faults, *Geophys. J. R. astr. Soc., 45*, 177-188, 1976

Meyer, Y.; *Wavelets and Applications*, Masson, 1992, and papers therein

Miltenberger, P., Sornette, D., Vanneste, C.; *Phys. Rev. Lett., 71*, 3604-3607, 1993

Mokhtar, T.A., Al-Saeed, M.M.; Shear wave velocity structures of the Arabian Peninsula, *Tectonophysics, 230*, 105-125, 1994

Mooney, W.D., Gettings, M.E., Blank, H.R., Healy, J.H.; Saudi Arabian seismic-refraction profile: a traveltime interpretation of crustal and upper mantle structure, *Tectonophysics, 111*, 173-246, 1985

Narr, W., Supe, J.; Joint spacing in sedimentary rocks, *J. Struct. Geol., 13*, 9, 1037-1048, 1991

Niazi, M.; Crustal thickness in the Central Saudi Arabian peninsula, *Geophys. J. R. Astr. Soc.; 15*, 545-547, 1968

Ord, A., Hobbs, B.E.; The strength of the continental crust, detachment zones and the development of plastic instabilities, *Tectonophysics, 158*,269-289, 1989

Ouillon, G.; *Application de l'analyse multifractale et de la transformée en ondelettes anisotropes à la caractérisation géométrique multi-échelle des réseaux de failles et de fractures*, Ph.D. Thesis, Nice University, France, 1995

Pollack, H.N., Hurter, S.J., Johnson, J.R.; Heat flow from the earth's interior: analysis of the global data set, *Rev. Geophys., 31*, 267-280, 1993

Pollard, D.D., Aydin, A.; Progress in understanding jointing over the past century, *Geol. Soc. Am. Bull., 100*, 1181-1204, 1988

Pollard, D.D., Segall, P.; Theoretical displacements and stresses near fractures in rock: with applications to faults, joints, veins, dikes, and solution surfaces', in *Fracture Mechanics of Rock*, B.C. Atkinson Editor, Academic Press, 1987

Prodehl, C.; Interpretation of a seismic-refraction survey across the Arabian shield in western Saudi Arabia, *Tectonophysics, 111*, 247-282, 1985

Ranalli, G.; *Rheology of the Earth*, Allen and Unwin, 1987

Roux, S., Hansen,A.; Introduction to multifractality, in *Disorder and Fracture*, J.C. Charmet, S. Roux, E. Guyon Editors, Plenum Press, 1990

Scholz, C.H.; *The Mechanics of Earthquakes and Faulting*, Cambridge University Press, 1990

Scholz, C.H., Aviles, C.A.; The fractal geometry of faults and faulting, in *Earthquake Source Mechanics*, Geophysical Monograph 37 (Maurice Ewing 6), Am. Geophys. Union, 1986

Scholz, C.H., Cowie, P.A.; determination of total strain from faulting using slip measurements, *Nature, 346*, 837-839, 1990

Segall, P., Pollard, D.P.; Joint formation in granitic rock of the Sierra Nevada , *Geol. Soc. of Am. Bull., 94*, 563-575, 1983

Sibson,, R.H; Earthquakes and rock deformation in crustal fault zones, *Ann. Rev. Earth Planet. Sci., 14*, 149-175, 1986

Sornette, A.; *Lois d'échelle dans les milieux fissurés, Ph. D. Thesis*, Université d'Orsay, France, 1990

Sornette, A., Davy, P., Sornette, D.; Growth of fractal fault patterns, *Phys. Rev. Lett., 65*, 2266-2269, 1990

Sornette, A., Davy, P., Sornette, D.; Fault growth in brittle-ductile experiments and the mechanics of continental collision, *J. Geophys. Res., 98*, B7, 12111-12137, 1993

Sornette, D.; Self-organized criticality in plate tectonics, in *Spontaneous formation of space-time structures and criticality*, T. Riste and D. Sherrington Editors, Kluwer Academic Publishers, 1991

Sornette, D., Davy, P.; Fault growth model and the universal length distribution, *Geophys. Res. Lett., 18*, 1079-1081, 1991

Tullis, J., Yund, R.A.; Experimental deformation of dry Westerly granite, *J. Geophys. Res., 82*, 36, 1977

Vaslet, D., Janjou, D., Robelin, C., Al Muallem, M.S., Halawani, M.A., Brosse, J.-M., Breton, J.-P., Courbouleix, S., Roobol, M.J., Dagain, J.; Explanatory notes to the geologic map of the Tayma quadrangle, sheet 27C, Kingdom of Saudi Arabia; Ministry of Petroleum and Mineral resources, Jiddah, Saudi Arabia, A.H. 1414, 1994

Villemin, T., Sunwoo, C.; Distribution logarithmique self-similaire des rejets et longueurs de failles: exemple du Bassin Houiller Lorrain, *C. R. Acad. Sci. Paris, 305, Série II*, 1309-1312, 1987

Walsh, J.J., Watterson, J.; Fractal analysis of fracture patterns using the standard box-counting technique: valid and invalid methodologies, *J. Struct. Geol., 15*, 12, 1509-1512, 1993

Wilson, K.G.; The renormalization group and critical phenomena, *Rev. of Mod. Phys., 55*, 3, 583-600, 1983

Witten, T.A., Sander, L.M.; *Phys. Rev. Lett., 47*, 1400-1403, 1981

Yeomans, J.M.; *Statistical mechanics of phase transitions*, Oxford Science Publications, 1992